



Hierarchically tailorable double-array film hybrids with enhanced photocatalytic and photoelectrochemical performances

Nan Zhang^{a,b}, Quan Quan^{a,b}, Ming-Yu Qi^{a,b}, Zi-Rong Tang^b, Yi-Jun Xu^{a,b,*}

^a State Key Laboratory of Photocatalysis on Energy and Environment, College of Chemistry, Fuzhou University, Fuzhou, 350116, PR China

^b College of Chemistry, New Campus, Fuzhou University, Fuzhou 350116, PR China

ARTICLE INFO

Keywords:

Double-array structure
TiO₂ nanotubes
ZnO nanorods
Reduced graphene oxide
Vectorial charge transfer

ABSTRACT

The basic mantra of “structure-dictates-function” in chemistry has inspired tremendous interests in designing various architectures toward specific applications. In this work, hierarchically tailorable double-array structures composed of TiO₂ nanotube arrays (TNTAs) and axially grown ZnO nanorod arrays (ZNRAs) have been constructed through a two-step anodization method combined with a heteroepitaxial growth process regulated by electrodeposited reduced graphene oxide (RGO). The obtained TNTAs/RGO/ZNRAs film hybrids exhibit enhanced photocatalytic and photoelectrochemical performances along with favorable photostability as compared to the single component and binary counterparts. This is ascribed to the synergistic effect of the matchable band alignment of the components, the 1D-on-1D double-array architecture with vectorial pathways for charge carriers transport, and the electrically conductive RGO for bridging the directional electron flow to further promote the separation and transfer of charge carriers. This work is anticipated to provide instructive recipe for rational design and construction of composite films with optimized photo(electro)catalytic performances.

1. Introduction

The growing depletion of fossil fuel reserves and the ever-increasing energy demand have stimulated intensive search for sustainable alternative energy [1,2]. A promising project lies in the design and construction of efficient semiconductor-based composites for the capture and conversion of solar energy into chemical energy via a renewable route [3,4]. Considering the significant impacts of the microscopic structure and morphology of catalysts on their overall performance, tuning the architectures of semiconductor-based materials is of paramount importance to optimize their activities toward photoredox applications [5–7].

One dimensional (1D) nanostructures, such as nanowires, nanotubes and nanorods, have attracted considerable interests due to their potential as building blocks for advanced technological applications, including dye-sensitized solar cells, field effect transistors, and photocatalysts [8–10]. Recent years have witnessed increasing interests in fabricating 1D semiconductors with controlled architectures [11–14]. Well-aligned 1D semiconductor arrays have been demonstrated to exhibit good electronic and optical properties, associated with directional mobility of charge carriers, large aspect ratio, decoupling directions of light absorption and quantum confinement effect [15–17]. These

features of 1D semiconductor arrays make them as favorable candidates for photocatalytic solar energy conversion [18,19].

Among the various 1D semiconductor arrays, TiO₂ nanotube and ZnO nanorod arrays have received great research attention owing to their unique optical and carrier transport performance as well as environmental friendliness [20–22]. For example, the light-harvesting efficiency and the electron diffusion length of TiO₂ nanotube arrays (TNTAs) are remarkably improved as compared with the nanoparticle counterparts due to the specific geometry advantages of TNTAs [23–25]. However, these semiconductors suffer from the drawback of high electron-hole recombination rate and thus low photoactivity [26]. To enhance the photocatalytic performance of 1D TiO₂ and ZnO nanoarrays, diverse approaches have been developed [11], among which the coupling of TiO₂ and ZnO to form type-II band alignment heterostructure provides an efficient strategy for improving the separation efficiency of photogenerated charge carriers [27,28]. Thus far, different TiO₂-ZnO hybrid 1D arrays structures have been reported, including TiO₂ nanorod-ZnO nanoparticle arrays [28,29], TiO₂ nanotube/ZnO nanoparticle core/shell arrays [30] and TiO₂ nanoparticles-coated ZnO nanorod arrays [31–33]. It is worth noting that 1D nanostructure is able to promote the electron transport by providing a direct path as compared to 0D nanoparticles [34–36]. Therefore, it is desirable to

* Corresponding author at: State Key Laboratory of Photocatalysis on Energy and Environment, College of Chemistry, Fuzhou University, Fuzhou, 350116, PR China.

E-mail address: yjxu@fzu.edu.cn (Y.-J. Xu).

<https://doi.org/10.1016/j.apcatb.2019.118086>

Received 19 June 2019; Accepted 13 August 2019

Available online 14 August 2019

0926-3373/ © 2019 Elsevier B.V. All rights reserved.

construct TiO_2 -ZnO arrayed hybrids with both components in 1D structures. In this context, ZnO nanorod grafted TiO_2 nanotube arrays [37,38] and branched hierarchical ZnO nanorod- TiO_2 nanotube array [39] have been synthesized. However, since the rapid charge transport property usually relies on the straight and axial conducting pathway provided by the 1D structure [40,41], designable 1D-on-1D semiconductor arrays in the parallel direction will be advantageous for the charge carriers transfer direction control, efficient separation of electron-hole pairs and thus enhanced solar energy conversion [42]. Therefore, 1D-on-1D semiconductor arrays along the axial direction represent favorable architectures for light trapping and charge carriers separation with optimized synergistic performance. However, the research in this regard is still lacking mainly because of the difficulty in controlling the growth orientation of secondary semiconductor arrays to obtain ordered 1D-on-1D nanostructure arrangement along the axial direction.

Herein, we report tailorable double-array hybrids consisting of highly ordered TiO_2 nanotube arrays (TNTAs) and axially grown ZnO nanorod arrays (ZNRAs) through a two-step anodization method combined with a heteroepitaxial growth process regulated by electrodeposited reduced graphene oxide (RGO). The architecture of the secondary ZNRAs in TNTAs/RGO/ZNRAs double arrays can be tuned by adjusting the growth condition of ZNRAs. The ternary TNTAs/RGO/ZNRAs hybrids exhibit higher photocatalytic activity toward organic pollutant degradation and better photoelectrochemical performance than the bare TNTAs, ZNRAs, and the binary counterparts. This results from the synergistic effect of the matchable band alignment of the components, the 1D-on-1D double-array structure providing vectorial pathways for charge carriers transport, and the electrically conductive RGO sheets for further facilitating the charge carriers separation. In addition, the recycling tests indicate that TNTAs/RGO/ZNRAs double arrays possess favorable photostability. This work is anticipated to promote further interests in the rational design and optimization of 1D semiconductor-based composite architectures with enhanced performances toward solar-energy-related applications.

2. Experimental section

2.1. Materials

Titanium foils (99.7% purity, 0.1 mm thickness), acetone ($\text{C}_3\text{H}_8\text{O}$), ethylene glycol ($\text{C}_2\text{H}_6\text{O}_2$), ammonium fluoride (NH_4F), nitric acid (HNO_3), graphite powder, hydrochloric acid (HCl), concentrated sulfuric acid (H_2SO_4 , 98%), potassium permanganate (KMnO_4), hydrogen peroxide (H_2O_2 , 30%), methanol (CH_3OH), zinc acetate dehydrate ($\text{C}_4\text{H}_6\text{O}_4\text{Zn} \cdot 2\text{H}_2\text{O}$), potassium hydroxide (KOH), zinc nitrate hexahydrate ($\text{Zn}(\text{NO}_3)_2 \cdot 6\text{H}_2\text{O}$), and hexamethylenetetramine ($\text{C}_6\text{H}_{12}\text{N}_4$). All of the reagents were used as received without further purification. The deionized water (DI water) used in the experiments was from local sources.

2.2. Preparation

2.2.1. Synthesis of TiO_2 nanotube arrays (TNTAs)

Highly ordered TNTAs were fabricated on $2\text{ cm} \times 1\text{ cm}$ Ti foils by a two-step anodization approach. Prior to anodization, Ti foils were cleaned by sonication in acetone, ethanol and DI water successively and dried with a N_2 stream. Anodic oxidation was conducted using a two-electrode system with the Ti foil as working electrode and a graphite sheet as counter electrode placed 3 cm apart. The electrolyte was ethylene glycol solution containing 0.3 wt% NH_4F and 2 vol% DI water. The first anodization was carried out at 50 V for 2 h and then the TNTAs were ultrasonically removed in DI water for 10 min. A second anodization was subsequently carried out at 50 V for 30 min using fresh electrolyte. The as-obtained TNTAs were washed by DI water and dried in air, finally annealed at 450 °C for 1 h in air with a heating rate of

2 °C min⁻¹.

2.2.2. Synthesis of TNTAs/RGO

Graphene oxide (GO) was synthesized from graphite powder by a modified Hummers' method. The detailed procedure was described in the Supporting Information. The cyclic voltammetric process was carried out in the 1.0 mg mL⁻¹ GO aqueous dispersion with a three-electrode system (the TNTAs/Ti as working electrode, Pt sheet as counter electrode and saturated calomel electrode (SCE) as reference electrode) on a CHI 760D electrochemical workstation. The scan was from -1.5 to 1 V at a rate of 50 mV s⁻¹. After deposition, the obtained TNTAs/RGO sample was washed with DI water and dried in air.

2.2.3. Synthesis of ZnO seeds

125 mL of zinc acetate dehydrate solution in methanol (0.01 M) was prepared under vigorous stirring at 60 °C. Then, 65 mL of KOH solution in methanol (0.03 M) was injected dropwise into the above solution. The sol-gel solution of ZnO seeds was obtained for the following reaction after continuous stirring at 60 °C for 2 h.

2.2.4. Synthesis of TNTAs/RGO/ZNRAs

As for the preparation of TNTAs/RGO/ZNRAs heterostructures, the TNTAs/RGO sample grown on the Ti foil was immersed into the as-obtained ZnO seed solution for 15 min and dried in air. Simultaneously, 150 mL of aqueous solution containing $\text{Zn}(\text{NO}_3)_2$ (0.02 M) and $\text{C}_6\text{H}_{12}\text{N}_4$ (0.02 M) was well dispersed by sonication in a round-bottom flask. Then, the TNTAs/RGO sample was placed into the bottom of the flask. The refluxing process was conducted at 90 °C for 2 h, 3 h or 4 h. The obtained TNTAs/RGO/ZNRAs samples were washed with DI water and dried at 60 °C.

2.2.5. Synthesis of TNTAs/ZnO

The preparation of TNTAs/ZnO follows the same procedure as that for TNTAs/RGO/ZNRAs except replacing TNTAs/RGO substrate with TNTAs.

2.2.6. Synthesis of ZnO on Ti foil

The preparation of bare ZnO on Ti foil follows the same procedure as that for TNTAs/RGO/ZNRAs except directly using Ti foil as the substrate.

2.3. Characterizations

The scanning electron microscopy (SEM) measurements were carried out using a ZEISS SIGMA scanning electron microscope with 20 kV accelerating voltage. An energy dispersive X-ray diffraction (XRD) patterns were recorded on a Panalytical X'pert Pro diffractometer using Cu K α radiation (40 kV, 30 mA). UV-vis diffuse-reflectance (DRS) spectra were recorded on a Varian-Cary 5000 spectrometer equipped with a diffuse-reflectance accessory, in which BaSO_4 was employed as a reference. X-ray photoelectron spectroscopy (XPS) measurements were operated on a Thermo Scientific ESCA Lab 250 spectrometer, which is made of a monochromatic Al K α as the X-ray source, a hemispherical analyzer, and sample stage with multiaxial adjustability to obtain the surface composition of the products. All the binding energies were calibrated by the C 1s peak at 284.6 eV.

2.4. Photoelectrochemical measurements

Photoelectrochemical measurements were carried out on a CHI electrochemical analyzer (CHI 760) using a standard three electrode mode. The Ti foils with samples ($1\text{ cm} \times 1\text{ cm}$) were used as the working electrode, a Pt sheet ($2\text{ cm} \times 2\text{ cm}$) and a saturated calomel electrode (SCE) served as counter electrode and reference electrode, respectively. The exposed area of the working electrode was 1 cm². A 300 W Xe arc lamp (PLS-SXE 300C, Beijing Perfectlight Co., Ltd.) was

employed as the irradiation source. The transient photocurrent responses experiments were conducted under on-off cycles of UV–vis light irradiation at 0.6 V vs. SCE in 0.1 M Na₂SO₄ aqueous solution. The linear-sweep voltammograms (LSV) experiments were performed at a scan rate of 0.01 V s⁻¹ in 0.1 M Na₂SO₄ aqueous solution under UV–vis light irradiation. The chopped LSV experiments were performed under on-off cycles of UV–vis light irradiation. The electrochemical impedance spectroscopy (EIS) experiments and the open circuit photovoltage (OCP) decay analysis were conducted using 0.2 M Na₂SO₄ aqueous solution as electrolyte. Incident photon-to-current conversion efficiency (IPCE) was collected by PEC-S20 (Peccell Technology Co. Ltd.) without bias potential and the light intensity was calibrated with a standard solar cell for amorphous silicon solar cell produced by Japan Quality Assurance Organization.

2.5. Photocatalytic activity

Photocatalytic activity was evaluated by using Rhodamine B (RhB) as a model organic dye pollutant compound. In a typical test, samples with the same area of 20 mm × 10 mm were soaked into 3.0 mL of RhB aqueous solution (5 mg/L) in a quartz cuvette. Before irradiation, the mixtures were kept in dark for 30 min to reach equilibrium of adsorption-desorption at room temperature. A 300 W Xe arc lamp (PLS-SXE 300C, Beijing Perfectlight Co., Ltd.) was employed as the irradiation source. A commercial electric fan was used to cool the reaction system. At each irradiation interval of 10 min, the concentration of RhB was determined by the absorbance of RhB at 553 nm.

3. Results and discussion

The fabrication procedure for the TNTAs/RGO/ZNRAs double-array structure is illustrated in Fig. 1. Highly ordered TiO₂ nanotube arrays (TNTAs) on the Ti foil prepared via a two-step electrochemical anodization method are used as building blocks. Graphene oxide (GO) nanosheets are electrochemically reduced and simultaneously electrodeposited onto TNTAs by cyclic voltammetry method to form TNTAs/RGO. After the deposition of ZnO seeds onto TNTAs/RGO via a surface adsorption process, ZnO nanorod arrays (ZNRAs) are vertically grown on the surface of TNTAs/RGO by a reflux condensation method to produce TNTAs/RGO/ZNRAs double-array film hybrids.

The morphologies of the samples have been observed by scanning electron microscopy (SEM). As shown in Fig. 2A, TNTAs are aligned on the Ti substrate with a thin layer of continuous nanoporous TiO₂ tiled on the top [43]. After the electrodeposition process, RGO nanosheets spread onto the TNTAs (Fig. 2B). The obtained TNTAs/RGO is used as a substrate for ZnO seeds deposition and subsequent heteroepitaxial growth of ZNRAs. It can be seen from Fig. 2C that in the TNTAs/RGO/

ZNRAs hybrid, ZNRAs are vertically grown on the surface of TNTAs/RGO to form a double-array structure. It should be noted that in the absence of RGO, the ZnO nanorods exhibit star-like morphology grown on the top of TNTAs instead of forming arrays, as displayed in Fig. 2D. These results indicate that the 2D RGO sheets provide a structure-directing platform for the heteroepitaxial growth and self-assembly of 1D ZnO nanorods into arrays, which is crucial for the construction of the desirable double-array structure.

The morphological evolution process of the TNTAs/RGO/ZNRAs heteroassemblies has been investigated by analyzing the morphology of the samples obtained with different reaction time for the growth of ZnO nanorod arrays (ZNRAs). It is seen from Fig. 3A that with the refluxing time of 2 h, the ZnO nanorods are formed sparsely on the surface of TNTAs/RGO and the uncovered RGO sheets can be clearly observed (the inset of Fig. 3A). The cross-section SEM image (Fig. 3B) reveals that the average length of ZNRAs is about 0.9 μm. When the refluxing time is prolonged to 3 h, the surface of RGO substrate is almost planted with ZnO nanorods (Fig. 3C) and ZNRAs are formed with the average length of ca. 1.2 μm (Fig. 3D). Further prolonged refluxing time (e.g., 4 h) leads to the dense gathering of ZnO nanorods on the surface of TNTAs/RGO and their average length grows to about 1.5 μm, as displayed in Fig. 3E and F. The SEM images reveal that the mild synthesis process of ZNRAs has no effect on the morphology of TNTAs/RGO substrate which maintains the oriented and uniform structure with the TiO₂ nanotube average length of 1.2 μm. These results indicate that ZnO nanorods are gradually grown on the surface of TNTAs/RGO during the refluxing process from slightly scattered distribution to compact arrays with the average length prolonged (Fig. 3G).

The compositional information and valence states of the elements in TNTAs/RGO/ZNRAs heterostructure (taking the sample obtained with the refluxing time of 3 h as an example) have been probed by X-ray photoelectron spectroscopy (XPS). The survey spectrum in Fig. 4A reveals the existence of C, Ti, O, and Zn elements in the TNTAs/RGO/ZNRAs composite. The successful reduction of GO to RGO by the electrodeposition process is verified by the C 1s spectrum (Fig. 4B), which displays a significant decrease of oxygen-containing functional groups as compared with that of the original GO (Fig. 4C). As shown in Fig. 4D, the binding energies of Ti 2p for Ti 2p_{3/2} and Ti 2p_{1/2} are determined to be 459.4 and 465.1 eV, respectively, which agrees with the Ti element in anatase TiO₂ (Ti⁴⁺) with a spin-orbit splitting value of 5.7 eV [44]. The high-resolution spectrum of Zn 2p in Fig. 4E exhibits two binding energy peaks at 1045.4 eV (Zn 2p_{1/2}) and 1022.4 eV (Zn 2p_{3/2}) with the spin-orbit splitting of 23.0 eV, which correspond to the chemical state of Zn²⁺ in ZnO [45]. With regard to the high-resolution spectrum of O 1s (Fig. 4F), the peak at 531.2 eV is attributed to the lattice oxygen of TiO₂ and ZnO (i.e., Ti–O and Zn–O) arising from the TNTAs and ZNRAs [46–48], and the peak at 532.9 eV is indexed to the

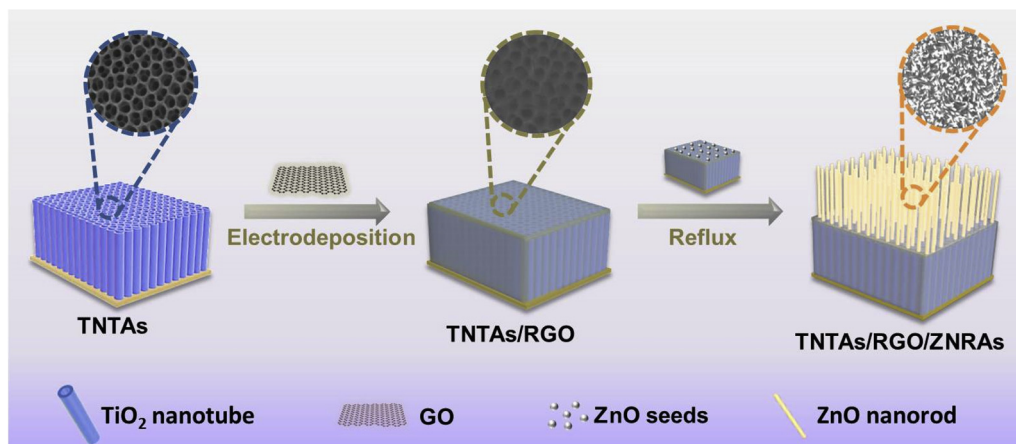


Fig. 1. Schematic illustration for the fabrication of TNTAs/RGO/ZNRAs double-array structure.

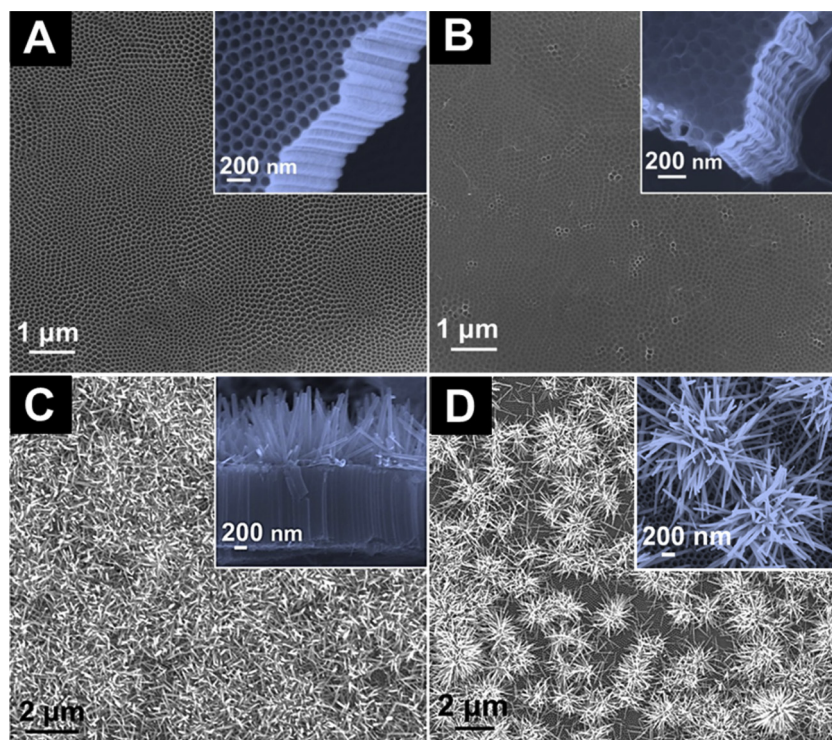


Fig. 2. SEM images of (A) TNTAs, (B) TNTAs/RGO, (C) TNTAs/RGO/ZNRAs double arrays, and (D) TNTAs/ZnO; the insets are the corresponding magnified SEM images in A,B,D and the cross-section SEM image in C.

oxygen in the adsorbed water and hydroxyl groups on the surface of the sample [49–51].

The crystallographic structures of the as-prepared samples have been analyzed by X-ray diffraction (XRD) spectra. As shown in Fig. 5A, besides the diffraction peaks from Ti foil (JCPDS card no. 44-1294), the diffraction peaks observed for the pristine TNTAs well match with anatase TiO_2 phase (JCPDS card no. 21-1272) [43]. The electro-deposition of RGO has no effect on the crystalline phase of TNTAs. No diffraction peaks of RGO can be observed in the composites, which should be ascribed to the relatively low diffraction intensity of RGO shielded by the strong diffraction peaks of anatase TiO_2 [52]. With the formation of ZNRAs onto TNTAs and TNTAs/RGO substrates, all diffraction peaks of TNTAs maintain and the additional diffraction peaks at 2θ values of 34.4° and 36.3° are indexed to (002) and (101) crystal planes of hexagonal phase ZnO (JCPDS card no. 36-1451), respectively [5].

The optical properties of the samples have been determined by UV–vis diffuse reflectance spectra (DRS) (Fig. 5B). The absorption onset of bare TNTAs is at approximately 390 nm. The visible-light absorption platform of TNTAs stems from the unique highly periodically porous structure and excellent morphology uniformity of TNTAs, which is in agreement with previous works [53–56]. With the introduction of RGO, the visible light absorption of TNTAs/RGO is enhanced as compared to TNTAs (Fig. S1) due to the intrinsic background absorption of RGO [57]. The deposition of ZnO nanorods onto TNTAs slightly decreases the absorbance of TNTAs/ZnO in the range of 400–600 nm, which is induced by the barely visible-light-response of ZnO directly grown on the Ti foil (Figs. S2 and S3), as demonstrated by its optical property (Fig. 5B) and the color of the samples (Fig. S4). The similar phenomenon has also been observed for the ternary TNTAs/RGO/ZNRAs composites and the absorbance decrease in the region of 400–600 nm becomes more significant as the reaction time for the growth of ZNRAs increases due to dense ZNRAs formed on the surface of TNTAs/RGO. The above results combined ascertain the successful assembly of double-array structure consisting of TNTAs, RGO, and ZNRAs.

Photocatalytic performances of the samples have been evaluated by

liquid-phase degradation of Rhodamine B (RhB), a common organic dye pollutant threatening water sources and human health [58,59]. As displayed in Fig. 5C, TNTAs/RGO exhibits enhanced adsorption capability than other samples, which is ascribed to the strong π – π interaction of exposed RGO deposited onto TNTAs with dye molecules [60,61]. Under UV–vis light irradiation, bare TNTAs and ZnO are photoactive for the degradation of RhB due to their band-gap-excitation by UV light. After deposition of RGO or ZnO onto TNTAs, the binary TNTAs/RGO and TNTAs/ZnO both exhibit higher photoactivity than TNTAs under the identical experimental conditions. Besides, the performance of TNTAs/ZnO composite also precedes that of bare ZnO directly grown on the Ti foil. The introduction of ZNRAs onto TNTAs/RGO leads to further enhanced photoactivity of the ternary composites with double-array structures as compared to the single component and binary counterparts. Besides, the performance of the ternary TNTAs/RGO/ZNRAs hybrids toward photocatalytic degradation of RhB can be tuned by employing different refluxing time for the growth of ZNRAs. Among the samples, TNTAs/RGO/ZNRAs obtained with the refluxing time of 3 h (denoted as TNTAs/RGO/ZNRAs-3 h) shows the highest photocatalytic activity toward degradation of RhB. The reaction rates of the samples have been calculated according to the pseudo-first-order model [62,63]. It is seen from Fig. S5 that the reaction rate of TNTAs/RGO/ZNRAs-3 h (0.0161 min^{-1}) is almost 1.8, 2.5, 1.6 and 1.5 times as high as those of TNTAs (0.0088 min^{-1}), ZnO (0.0065 min^{-1}), TNTAs/RGO (0.0103 min^{-1}) and TNTAs/ZnO (0.0110 min^{-1}), respectively, which is comparable or superior to the typical TNTAs-based photocatalysts toward degradation of RhB in the previous reports (Table S1). Blank experiment performed under UV–vis light irradiation in the absence of photocatalysts demonstrates negligible activity, indicating that the degradation reaction is driven by the photocatalysts. In addition, the photostability of the samples has been studied. It is seen from Fig. 5D that the bare ZnO exhibits obvious loss of photoactivity after six recycling tests for degradation of RhB under UV–vis light irradiation, which could be ascribed to the photocorrosion of ZnO [64]. Notably, no significant loss of photoactivity is observed over TNTAs/RGO/ZNRAs-3 h during six successive recycling tests. Besides, there are no

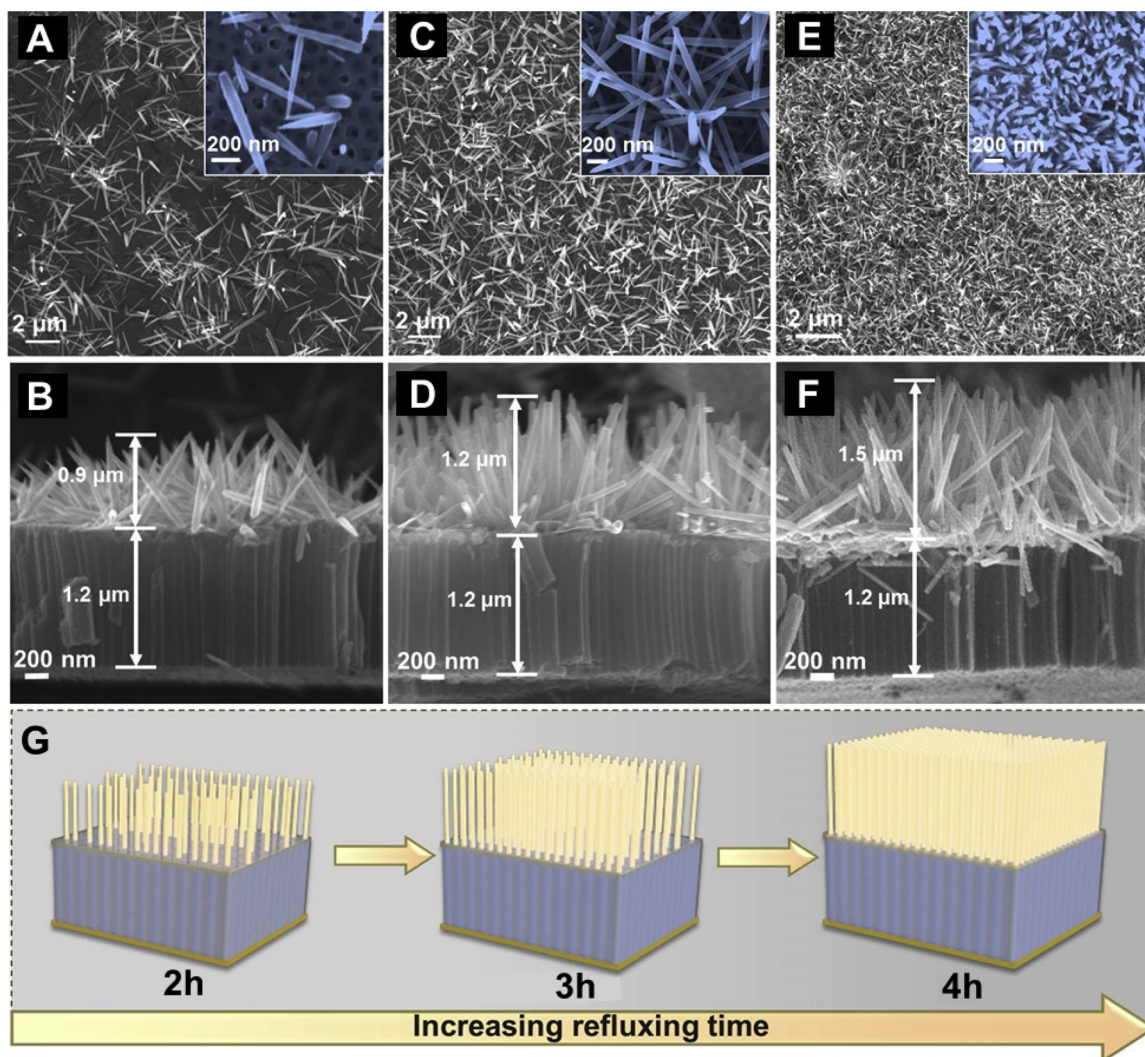


Fig. 3. SEM images of the TNTAs/RGO/ZNRs samples obtained with different refluxing time for the growth of ZNRs: (A, B) 2 h, (C, D) 3 h, and (E, F) 4 h; the first row is the top-surface SEM images with magnified images in the insets; the second row is the corresponding cross-section SEM images; (G) schematic illustration for the evolution of TNTAs/RGO/ZNRs heteroassemblies obtained with different refluxing time.

observable changes in its morphology (Fig. S6) and crystalline phase (Fig. S7) after the photocatalytic reaction. These results demonstrate that the photocorrosion of ZnO is effectively inhibited by constructing such double-array nanostructure.

Then photoelectrochemical measurements have been performed using the samples as photoanodes. The linear sweep voltammograms (LSV) in Fig. 6A show that the bare TNTAs and ZnO display relatively low photoresponse over the wide potential window under UV–vis light irradiation. The introduction of RGO onto TNTAs leads to the increased photocurrent density of TNTAs/RGO due to the electrically conductive property of RGO [65]. With the construction of TNTAs/ZnO heterostructure, higher photocurrent density than bare TNTAs and ZnO is obtained. The ternary TNTAs/RGO/ZNRs double-array structures exhibit further enhanced photocurrent density. It is observed that the photocurrent density of the ternary composites obtained with different refluxing time for ZNRs growth follows the order as: TNTAs/RGO/ZNRs-3 h > TNTAs/RGO/ZNRs-2 h > TNTAs/RGO/ZNRs-4 h, which is consistent with the trend of their photoactivity. These results indicate that the density and length of ZnO nanorods affect the efficiency of the charge carriers transfer in the double-array structure, which in turn influences their photoelectrochemical properties as well as the photocatalytic performances. Furthermore, the transient photocurrent measurements and chronoamperometry plots under chopped

UV–vis light illumination have also been conducted. As displayed in Fig. 6B and C, all the samples display a prompt photocurrent response with respect to the on-off cycles of the irradiation and the current density of the electrodes follows the same trend as the LSV results (Fig. 6A). The reproducible and steady photocurrent density of the TNTAs/RGO/ZNRs composites indicate the good photochemical stability of the electrodes [66]. Fig. 6D shows the incident photon-to-current conversion efficiency (IPCE) spectra of the samples. It can be seen that all samples have an absorption edge at *ca.* 400 nm. The introduction of RGO into TNTAs can enhance the IPCE over the UV region, which is ascribed to the electron acceptor role of RGO to promote the separation of electron-hole pairs [57]. TNTAs/ZnO exhibits higher IPCE than bare TNTAs and ZnO due to their matched band structure for efficient charge carriers separation [27,28]. The construction of ternary double-array structures is able to further improve the IPCE response as compared to the binary TNTAs/RGO and TNTAs/ZnO, suggesting more efficient separation and transportation of photogenerated charge carriers achieved in TNTAs/RGO/ZNRs.

To gain further insight into the origin of enhanced performances of the ternary TNTAs/RGO/ZNRs double-array composites, more characterizations have been carried out to comparatively investigate the charge carriers separation and transfer processes of the samples. The open circuit photovoltage (OCP) decay analysis (Fig. 7A) has been

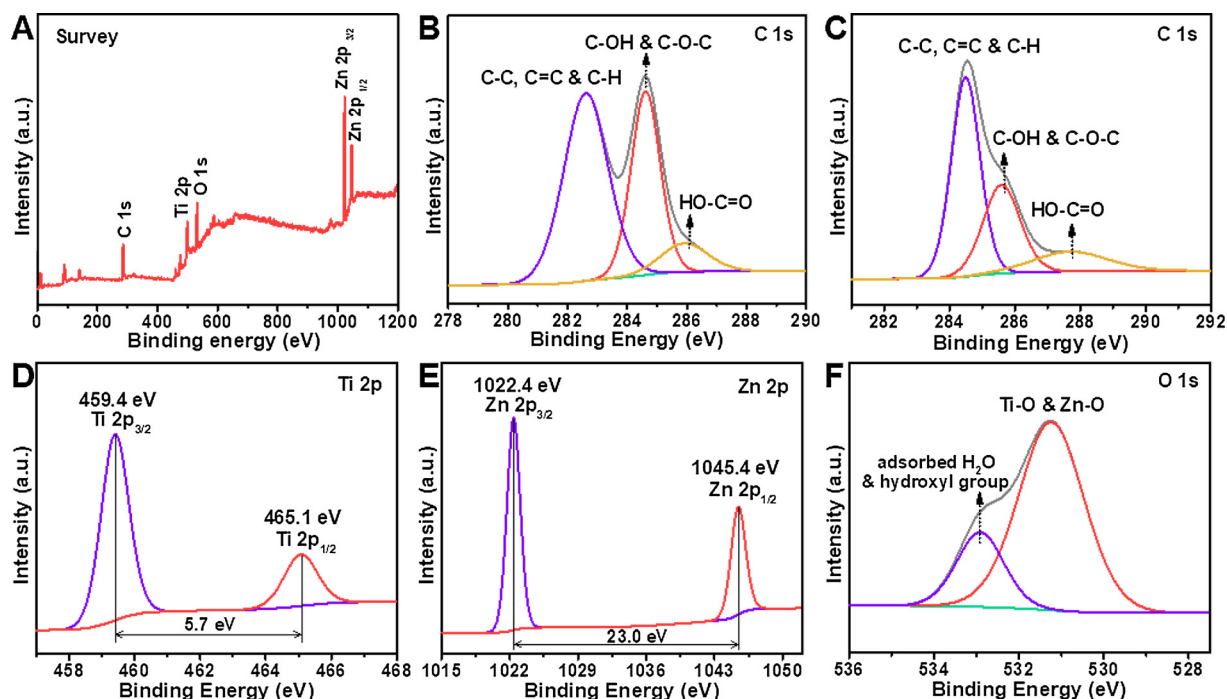


Fig. 4. (A) XPS survey spectrum of TNTAs/RGO/ZNRs composite; high-resolution XPS C 1s spectra of (B) TNTAs/RGO/ZNRs and (C) the original GO; high-resolution XPS spectra of (D) Ti 2p, (E) Zn 2p and (F) O 1s for TNTAs/RGO/ZNRs composite.

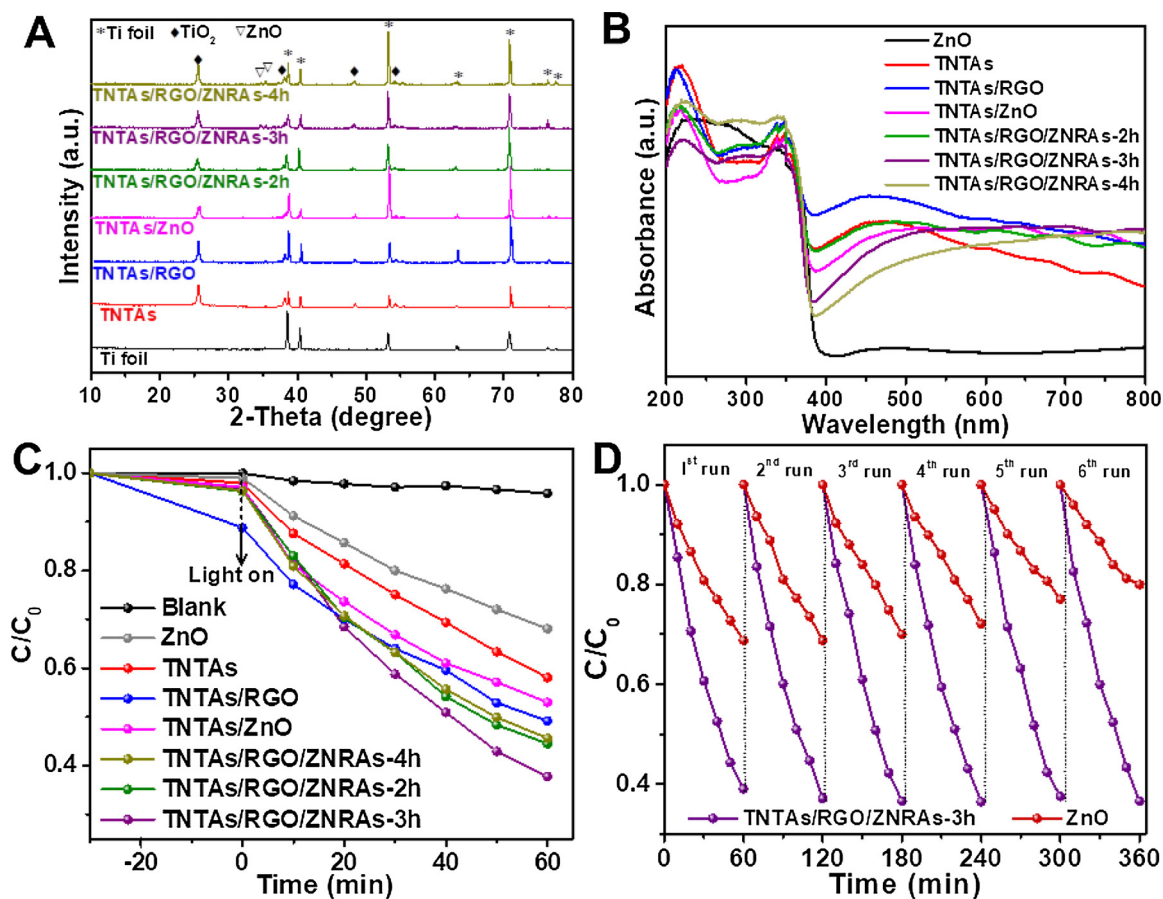


Fig. 5. (A) X-ray diffraction (XRD) spectra, (B) UV-vis diffuse reflectance spectra (DRS) and (C) photocatalytic performances for degradation of RhB under UV-vis light irradiation over the samples (TNTAs/RGO/ZNRs composites obtained with different refluxing time are denoted as TNTAs/RGO/ZNRs-x; x is the refluxing time); (D) recycling photodegradation of RhB under the irradiation of UV-vis light over TNTAs/RGO/ZNRs-3 h and ZnO.

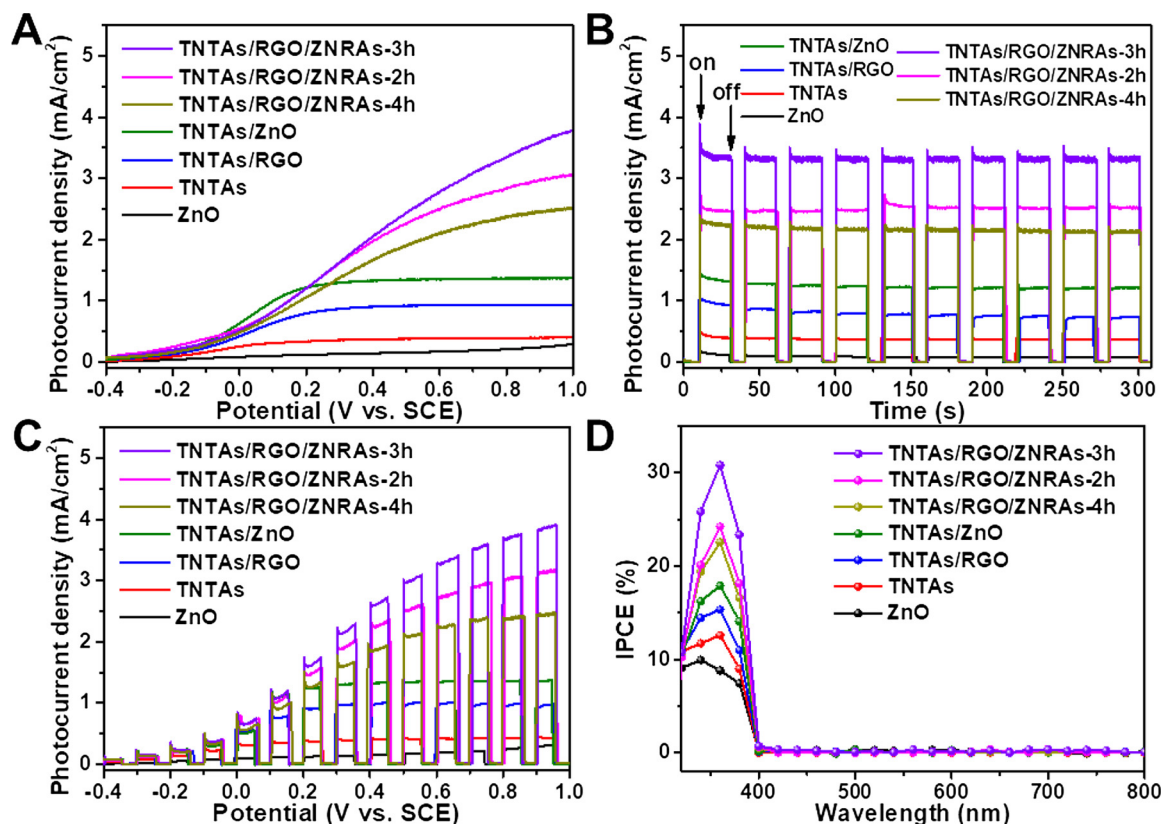


Fig. 6. (A) Linear-sweep voltammograms (LSV) of the samples under the irradiation of UV-vis light; (B) transient photocurrent responses and (C) LSV results of the samples under chopped light illumination; (D) incident photon-to-current conversion efficiency (IPCE) spectra of the samples under monochromatic light irradiation.

applied to assess the lifetime of photoelectrons by monitoring the decay of photovoltage (V_{oc}) with time after turning off the illumination at a steady state of the V_{oc} [67]. The photoelectron lifetime (τ) is estimated according to the following equation [68]:

$$\tau = -\frac{k_B T}{e} \left(\frac{dV_{oc}}{dt} \right)^{-1}$$

where k_B is Boltzmann's constant, T is the temperature, e is the elementary electronic charge, and V_{oc} is the open-circuit voltage at time t . The calculated electron lifetime as a function of V_{oc} is shown in Fig. 7B.

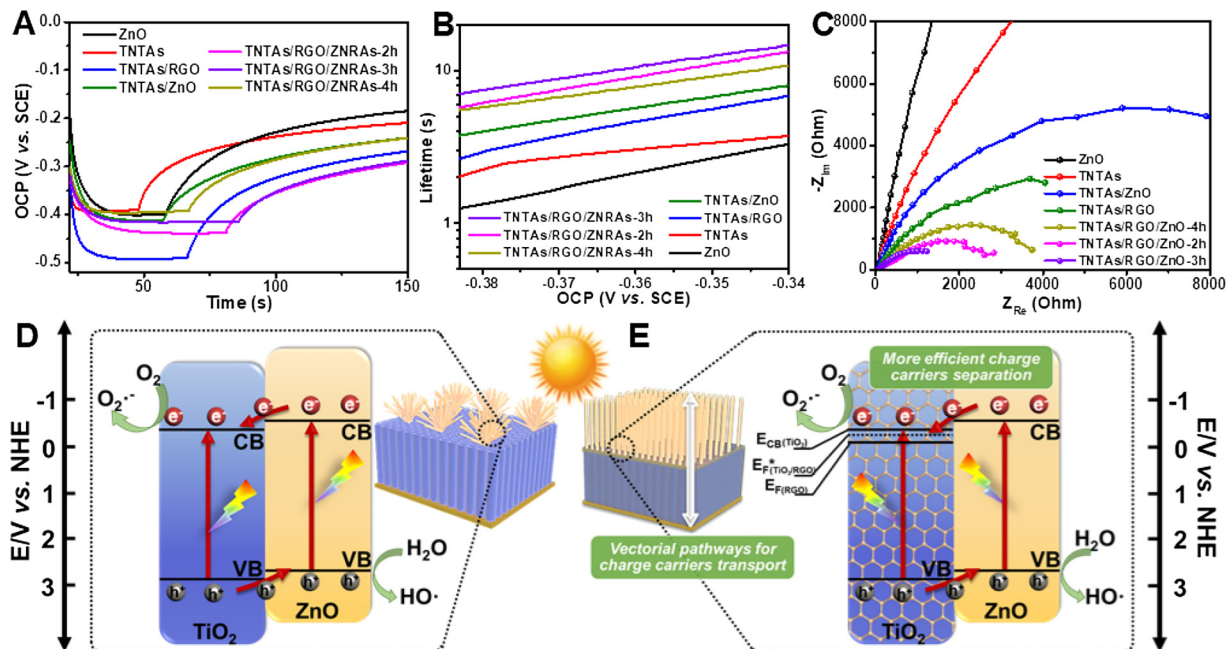


Fig. 7. (A) Illuminated open circuit potential (OCP) and (B) electron lifetime determined from the decay of OCP in dark of the samples; (C) Nyquist plots of the sample electrodes; schematic illustrations of the charge carriers transfer over (D) binary TNTAs/ZnO and (E) ternary TNTAs/RGO/ZNRAs double-array structure.

As is clearly seen, the ternary TNTAs/RGO/ZNRAs exhibit prolonged lifetime of photoelectrons as compared with bare TNTAs, ZnO, binary TNTAs/RGO and TNTAs/ZnO counterparts. The trend is in accordance with the photocatalytic and photoelectrochemical performances of the samples. The electrochemical impedance spectroscopy (EIS) has been used to characterize the charge carriers migration at the interface between electrolyte and the electrodes [69,70]. As displayed in Fig. 7C, the Nyquist plots of the samples exhibit semicircles at high frequencies, which are corresponding to the kinetic control model and ascribed to the double-layer capacitance (C_{dl}) in parallel with the charge transfer resistance (R_{ct}) at the contact interface between electrode and electrolyte [71]. The ternary TNTAs/RGO/ZNRAs composites possess smaller semicircular diameter than the single and binary counterparts. TNTAs/RGO/ZNRAs-3 h has the smallest semicircular diameter and thus the smallest charge transfer resistance between the electrode and electrolyte among the samples. These results manifest that the construction of optimized double-array structure and the introduction of RGO are able to synergistically improve the charge carriers separation and transportation in the composites and thus enhance their photocatalytic and photoelectrochemical performances.

Accordingly, a tentative reaction mechanism for photocatalytic degradation of RhB over the ternary TNTAs/RGO/ZNRAs composite has been proposed. As illustrated in Fig. 7D, under UV-vis light irradiation, both TiO_2 and ZnO are band-gap-excited to produce electron-hole pairs. The photogenerated electrons in the conduction band (CB) of ZnO are inclined to transfer to the CB of TiO_2 and meanwhile, the holes in the valence band (VB) of TiO_2 transfer to the VB of ZnO owing to their matchable energy band structures [39]. Thus the efficient separation of charge carriers photogenerated in TiO_2 and ZnO is realized. The introduction of RGO nanosheets onto TNTAs has two-folded effects. On one hand, the RGO nanosheets provide a growing platform for ZNRAs axially onto TNTAs substrate (Fig. 7E). Such double-array nanostructures promote efficient separation and transport of charge carriers along the longitudinal direction of the 1D-on-1D architecture. On the other hand, the RGO with high work function (i.e., -0.08 V versus-normal hydrogen electrode, NHE) [57] can positively shift the apparent Fermi level (E_F^*) of TNTAs/RGO due to the Fermi-level equilibration [72,73] (Fig. 7E). Under such conditions, the electron transfer from the CB of ZnO to the TNTAs/RGO substrate is more efficient, as demonstrated by the enhanced photocurrent response of the ternary TNTAs/RGO/ZNRAs composite as compared to the binary TNTAs/ZnO counterpart. The separated electrons and holes directly take part in the degradation of RhB molecules, and react with dissolved oxygen and water to produce superoxide radical anions ($\text{O}_2^{\cdot-}$) and hydroxyl radicals (O^{\cdot}H), respectively. These active radicals are involved in the process for RhB degradation, as indicated by the control experiments with the addition of different radical scavengers (Fig. S8).

4. Conclusions

In summary, the hierarchical TNTAs/RGO/ZNRAs double-array film hybrids have been constructed through a two-step anodization method and a heteroepitaxial growth process tuned by RGO nanosheets. The matched energy band structure of TNTAs and ZNRAs, and the specific double-array heterostructure enable the efficient separation and transport of charge carriers with vectorial pathways. The electrically conductive RGO bridges the directional electron flow to further promote the charge carriers separation due to its high work function to positively shift the apparent Fermi level of TNTAs/RGO substrate. The synergistic effect of these aspects endows the TNTAs/RGO/ZNRAs composites with improved photocatalytic activity for degradation of organic pollutant and photoelectrochemical performance as compared with bare TNTAs, ZnO nanorods, binary TNTAs/RGO and TNTAs/ZnO counterparts. This work suggests the wide scope of rational design and construction of 1D semiconductor-based composite architectures toward the optimization of performances for solar energy conversion.

Declaration of Competing Interest

The authors declare that they have no known competing financial interests or personal relationships that could have appeared to influence the work reported in this paper.

Acknowledgements

The support from the NSFC (U1463204, 21173045, 21872029 and 21802020), the Award Program for Minjiang Scholar Professorship, the Independent Research Project of State Key Laboratory of Photocatalysis on Energy and Environment (NO. 2014A05), the 1st Program of Fujian Province for Top Creative Young Talents, the NSF of Fujian Province for Distinguished Young Investigator Rolling Grant (2017J07002), the National Postdoctoral Program for Innovative Talents (BX201700053), and the China Postdoctoral Science Foundation (2017M622052) is gratefully acknowledged.

Appendix A. Supplementary data

Supplementary material related to this article can be found, in the online version, at doi:<https://doi.org/10.1016/j.apcatb.2019.118086>.

References

- [1] X. Chen, C. Li, M. Grätzel, R. Kostecki, S.S. Mao, Chem. Soc. Rev. 41 (2012) 7909–7937.
- [2] C. Ampelli, G. Centi, R. Passalacqua, S. Perathoner, Energy Environ. Sci. 3 (2010) 292–301.
- [3] Q. Quan, X. Lin, N. Zhang, Y.-J. Xu, Nanoscale 9 (2017) 2398–2416.
- [4] F.-X. Xiao, M. Pagliaro, Y.-J. Xu, B. Liu, Chem. Soc. Rev. 45 (2016) 3088–3121.
- [5] C. Han, Z. Chen, N. Zhang, J.C. Colmenares, Y.-J. Xu, Adv. Funct. Mater. 25 (2015) 221–229.
- [6] P.V. Kamat, J. Phys. Chem. C 112 (2008) 18737–18753.
- [7] S. Rawalekar, T. Mokari, Adv. Energy Mater. 3 (2013) 12–27.
- [8] B. Liu, E.S. Aydil, J. Am. Chem. Soc. 131 (2009) 3985–3990.
- [9] S.S. Warule, N.S. Chaudhari, J.D. Ambekar, B.B. Kale, M.A. More, ACS Appl. Mater. Interfaces 3 (2011) 3454–3462.
- [10] Y. Xia, P. Yang, Y. Sun, Y. Wu, B. Mayers, B. Gates, Y. Yin, F. Kim, H. Yan, Adv. Mater. 15 (2003) 353–389.
- [11] S. Liu, Z.-R. Tang, Y. Sun, J.C. Colmenares, Y.-J. Xu, Chem. Soc. Rev. 44 (2015) 5053–5075.
- [12] W. Guo, C. Xu, G. Zhu, C. Pan, C. Lin, Z.L. Wang, Nano Energy 1 (2012) 176–182.
- [13] D. Agarwal, C.O. Aspetti, M. Cargnello, M. Ren, J. Yoo, C.B. Murray, R. Agarwal, Nano Lett. 17 (2017) 1839–1845.
- [14] S. Liu, M.-Q. Yang, Z.-R. Tang, Y.-J. Xu, Nanoscale 6 (2014) 7193–7198.
- [15] Q. Simon, D. Barreca, A. Gasparotto, C. Maccato, T. Montini, V. Gombac, P. Fornasiero, O.I. Lebedev, S. Turner, G. Van Tendeloo, J. Mater. Chem. 22 (2012) 11739–11747.
- [16] S. Liu, C. Han, Z.-R. Tang, Y.-J. Xu, Mater. Horiz. 3 (2016) 270–282.
- [17] X. Feng, K. Shankar, O.K. Varghese, M. Paulose, T.J. Latempa, C.A. Grimes, Nano Lett. 8 (2008) 3781–3786.
- [18] M. Ge, Q. Li, C. Cao, J. Huang, S. Li, S. Zhang, Z. Chen, K. Zhang, S.S. Al-Deyab, Y. Lai, Adv. Sci. 4 (2017) 1600152.
- [19] X. Lin, S.-H. Li, K.-Q. Lu, Z.-R. Tang, Y.-J. Xu, New J. Chem. 42 (2018) 14096–14103.
- [20] Z.R. Tian, J.A. Voigt, J. Liu, B. McKenzie, H. Xu, J. Am. Chem. Soc. 125 (2003) 12384–12385.
- [21] K. Shankar, J.I. Basham, N.K. Allam, O.K. Varghese, G.K. Mor, X. Feng, M. Paulose, J.A. Seabold, K.-S. Choi, C.A. Grimes, J. Phys. Chem. C 113 (2009) 6327–6359.
- [22] K.S. Ranjith, R. Pandian, E. McGlynn, R.T. Rajendra Kumar, Cryst. Growth Des. 14 (2014) 2873–2879.
- [23] K. Zhu, N.R. Neale, A. Miedaner, A.J. Frank, Nano Lett. 7 (2007) 69–74.
- [24] I. Paramasivam, H. Jha, N. Liu, P. Schmuki, Small 8 (2012) 3073–3103.
- [25] R.P. Lynch, A. Ghicov, P. Schmuki, J. Electrochem. Soc. 157 (2010) G76–G84.
- [26] Y.-S. Xie, L. Yuan, N. Zhang, Y.-J. Xu, Appl. Catal. B 238 (2018) 19–26.
- [27] S. Hernández, V. Cauda, A. Chiodoni, S. Dallorto, A. Sacco, D. Hidalgo, E. Celasco, C.F. Pirri, ACS Appl. Mater. Interfaces 6 (2014) 12153–12167.
- [28] S. Hu, B. Wang, M. Zhu, Y. Ma, Z. Lv, H. Wang, Appl. Surf. Sci. 403 (2017) 126–132.
- [29] S. Hu, B. Wang, M. Zhu, Y. Ma, J. Wang, Energy Technol. 5 (2017) 1599–1605.
- [30] A. Sarkar, A.K. Singh, G.G. Khan, D. Sarkar, K. Mandal, RSC Adv. 4 (2014) 55629–55634.
- [31] Z. He, Y. Li, Q. Zhang, H. Wang, Appl. Catal. B 93 (2010) 376–382.
- [32] R. Wang, H. Tan, Z. Zhao, G. Zhang, L. Song, W. Dong, Z. Sun, J. Mater. Chem. A 2 (2014) 7313–7318.
- [33] M. Kwiatkowski, I. Bezverkhyy, M. Skompska, J. Mater. Chem. A 3 (2015) 12748–12760.
- [34] M. Law, L.E. Greene, J.C. Johnson, R. Saykally, P. Yang, Nat. Mater. 4 (2005)

- 455–459.
- [35] Y. Bai, H. Yu, Z. Li, R. Amal, G.Q. Lu, L. Wang, *Adv. Mater.* 24 (2012) 5850–5856.
- [36] T. Hu, L. Chen, Z. Deng, Y. Chen, *J. Mater. Chem. A* 3 (2015) 10890–10899.
- [37] Y.-C. Huang, S.-Y. Chang, C.-F. Lin, W.J. Tseng, *J. Mater. Chem.* 21 (2011) 14056–14061.
- [38] Y. Lei, G. Zhao, M. Liu, Z. Zhang, X. Tong, T. Cao, *J. Phys. Chem. C* 113 (2009) 19067–19076.
- [39] F.-X. Xiao, S.-F. Hung, H.B. Tao, J. Miao, H.B. Yang, B. Liu, *Nanoscale* 6 (2014) 14950–14961.
- [40] X. Sheng, D. He, J. Yang, K. Zhu, X. Feng, *Nano Lett.* 14 (2014) 1848–1852.
- [41] J. Tian, Z. Zhao, A. Kumar, R.I. Boughton, H. Liu, *Chem. Soc. Rev.* 43 (2014) 6920–6937.
- [42] X. Wang, C. Liow, A. Bisht, X. Liu, T.C. Sum, X. Chen, S. Li, *Adv. Mater.* 27 (2015) 2207–2214.
- [43] Q. Quan, S. Xie, B. Weng, Y. Wang, Y.-J. Xu, *Small* 14 (2018) 1704531.
- [44] C. Hsu, Y. Shen, Z. Wei, D. Liu, F. Liu, *J. Alloys Compd.* 613 (2014) 117–121.
- [45] S.-M. Lam, J.-C. Sin, I. Satoshi, A.Z. Abdullah, A.R. Mohamed, *Appl. Catal. A* 471 (2014) 126–135.
- [46] A. Jitianu, T. Cacciaguerra, M.-H. Berger, R. Benoit, F. Béguin, S. Bonnamy, *J. Non-Cryst. Solids* 345–346 (2004) 596–600.
- [47] X. Yan, C. Zou, X. Gao, W. Gao, *J. Mater. Chem.* 22 (2012) 5629–5640.
- [48] Y. Ku, Y.-H. Huang, Y.-C. Chou, *J. Mol. Catal. A: Chem.* 342–343 (2011) 18–22.
- [49] S. Guo, Y. Zhu, Y. Yan, Y. Min, J. Fan, Q. Xu, *Appl. Catal. B* 185 (2016) 315–321.
- [50] J.T. Klopogge, L.V. Duong, B.J. Wood, R.L. Frost, *J. Colloid Interface Sci.* 296 (2006) 572–576.
- [51] K. Wang, C. Shao, X. Li, F. Miao, N. Lu, Y. Liu, *Materials* 9 (2016) 90.
- [52] Y. Zhang, Z.-R. Tang, X. Fu, Y.-J. Xu, *ACS Nano* 4 (2010) 7303–7314.
- [53] G.K. Mor, O.K. Varghese, M. Paulose, K. Shankar, C.A. Grimes, *Sol. Energy Mater. Sol. Cells* 90 (2006) 2011–2075.
- [54] H.-F. Zhuang, C.-J. Lin, Y.-K. Lai, L. Sun, J. Li, *Environ. Sci. Technol.* 41 (2007) 4735–4740.
- [55] Y. Lai, L. Sun, Y. Chen, H. Zhuang, C. Lin, J.W. Chin, *J. Electrochem. Soc.* 153 (2006) D123–D127.
- [56] F.-X. Xiao, S.-F. Hung, J. Miao, H.-Y. Wang, H. Yang, B. Liu, *Small* 11 (2015) 554–567.
- [57] N. Zhang, M.-Q. Yang, S. Liu, Y. Sun, Y.-J. Xu, *Chem. Rev.* 115 (2015) 10307–10377.
- [58] B. Cheng, Y. Le, J. Yu, *J. Hazard. Mater.* 177 (2010) 971–977.
- [59] F. Mushtaq, A. Asani, M. Hoop, X.-Z. Chen, D. Ahmed, B.J. Nelson, S. Pané, *Adv. Funct. Mater.* 26 (2016) 6995–7002.
- [60] Z. Xiong, L.L. Zhang, J. Ma, X.S. Zhao, *Chem. Commun.* 46 (2010) 6099–6101.
- [61] Y. Liu, X. Jiang, B. Li, X. Zhang, T. Liu, X. Yan, J. Ding, Q. Cai, J. Zhang, *J. Mater. Chem. A* 2 (2014) 4264–4269.
- [62] A. Zhu, Q. Zhao, X. Li, Y. Shi, *ACS Appl. Mater. Interfaces* 6 (2014) 671–679.
- [63] N. Zhang, S. Liu, X. Fu, Y.-J. Xu, *J. Phys. Chem. C* 115 (2011) 9136–9145.
- [64] C. Han, M.-Q. Yang, B. Weng, Y.-J. Xu, *Phys. Chem. Chem. Phys.* 16 (2014) 16891–16903.
- [65] X. Xie, K. Kretschmer, G. Wang, *Nanoscale* 7 (2015) 13278–13292.
- [66] F. Ning, M. Shao, S. Xu, Y. Fu, R. Zhang, M. Wei, D.G. Evans, X. Duan, *Energy Environ. Sci.* 9 (2016) 2633–2643.
- [67] S.-F. Hung, F.-X. Xiao, Y.-Y. Hsu, N.-T. Suen, H.-B. Yang, H.M. Chen, B. Liu, *Adv. Energy Mater.* 6 (2016) 1501339.
- [68] B.H. Meekins, P.V. Kamat, *ACS Nano* 3 (2009) 3437–3446.
- [69] F. Fabregat-Santiago, G. Garcia-Belmonte, J. Bisquert, A. Zaban, P. Salvador, *J. Phys. Chem. B* 106 (2002) 334–339.
- [70] N.J. Bell, Y.H. Ng, A. Du, H. Coster, S.C. Smith, R. Amal, *J. Phys. Chem. C* 115 (2011) 6004–6009.
- [71] H.-L. Guo, X.-F. Wang, Q.-Y. Qian, F.-B. Wang, X.-H. Xia, *ACS Nano* 3 (2009) 2653–2659.
- [72] N. Zhang, Y. Zhang, X. Pan, M.-Q. Yang, Y.-J. Xu, *J. Phys. Chem. C* 116 (2012) 18023–18031.
- [73] X. Yu, J. Zhang, Z. Zhao, W. Guo, J. Qiu, X. Mou, A. Li, J.P. Claverie, H. Liu, *Nano Energy* 16 (2015) 207–217.